Journal of Energy Chemistry 54 (2021) 242–253

Contents lists available at ScienceDirect

Journal of Energy Chemistry

journal homepage: www.elsevier.com/locate/jechem

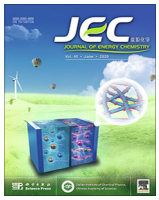

Review

Advances in *in-situ* characterizations of electrode materials for better supercapacitors

Xiaoli Su, Jianglin Ye, Yanwu Zhu *

Hefei National Research Center for Physical Sciences at the Microscale, & Department of Materials Science and Engineering, & CAS Key Laboratory of Materials for Energy Conversion, & i-ChEM, University of Science and Technology of China, Hefei 230026, Anhui, China

ARTICLE INFO

Article history:
Received 21 March 2020
Revised 24 May 2020
Accepted 26 May 2020
Available online 4 June 2020

Keywords:
Electric double layer capacitor
Pseudocapacitor
In-situ technique
Charge storage mechanism

ABSTRACT

In past decades, the performance of supercapacitors has been greatly improved by rationalizing the electrode materials at the nanoscale. However, there is still a lack of understanding on how the charges are efficiently stored in the electrodes or transported across the electrolyte/electrode interface. As it is very challenging to investigate the ion-involved physical and chemical processes with single experiment or computation, combining advanced analytic techniques with electrochemical measurements, *i.e.*, developing *in-situ* characterizations, have shown considerable prospect for the better understanding of behaviors of ions in electrodes for supercapacitors. Herein, we briefly review several typical *in-situ* techniques and the mechanisms these techniques reveal in charge storage mechanisms specifically in supercapacitors. Possible strategies for designing better electrode materials are also discussed.

Contents

* Corresponding author.
E-mail address: zhuyanwu@ustc.edu.cn (Y. Zhu).

https://doi.org/10.1016/j.jechem.2020.05.055

Xiaoli Su received her master degree from Zheng Zhou University in 2018. After that, she continued her study at the University of Science and Technology of China as a PhD candidate, under the supervision of Prof. Yanwu Zhu. Her main research interests are the chemical activation mechanism and the electrochemical properties of porous carbons for supercapacitors.

Jianglin Ye is a PhD candidate at the University of Science and Technology of China. His research is mainly focused on the synthesis of novel carbon materials such as graphene for supercapacitors, and the related charging mechanisms for efficient energy storage.

Yanwu Zhu joined the University of Science and Technology of China as a full professor in 2011. Prior to this, he obtained his PhD degree in physics from National University of Singapore in 2007. Then he worked as a postdoctoral fellow sequentially at National University of Singapore and at the University of Texas at Austin. His current research interest is the synthesis of novel carbon nanomaterials and their applications for energy storage and conversion.

1. Introduction

A significant increase in the worldwide consumption of fossil fuels, resulting from the rapid growth of the global economy, has been accelerating the exhaustion of fossil fuel reservation and the deterioration of environmental problems [1,2]. Hence, the renewable energy generated, *e.g.*, from the sun and wind, as well as electric vehicles with low CO_2 emissions, have been widespread concerned, for which the energy storage system is expected to act as the basic unit in power supply [3,4]. In this regard, batteries and electrochemical supercapacitors are recognized as the two important energy storage devices. Electrochemical capacitors, also known as supercapacitors, are a type of devices featured with high power density and long life time [3,5]. According to the different working principles, supercapacitors are classified as electric double layer capacitors (EDLCs) and pseudocapacitors, in which the former store energy by physical absorption of ions on the electrode while reversible redox reactions occur in electrodes of pseudocapacitors.

In observation of the importance of electrodes for the supercapacitor performances, preparing novel electrode materials or modifying the current electrode materials by processing techniques, has been extensively considered to improve the performance of supercapacitors. Among various materials, carbon materials such as activated carbons, carbon nanotubes, carbide-derived carbons and graphene, have been investigated as electrode materials for EDLCs because of low density, high conductivity, high specific surface area (SSA) and good chemical stability [6]. Comparatively, metal oxides and conductive polymers exhibit pseudocapacitive behaviors and have attracted intensive attention because of the larger capacity, low-cost, easy preparation, light weight and high flexibility [7]. Recently, two-dimensional (2D) materials other than graphene, *e.g.*, MXenes, have attracted intensive interest as supercapacitor electrodes since MXenes comprise a conductive carbide core and a redox surface [2,5]. Table 1 lists the state-of-the-art of the electrode material performances in terms of specific capacitance and cycling lifetime, with testing methods indicated. As we can see, conductive polymers own specific capacities much higher than bare carbons, but typically with limited scan rate and lifetime. On the other hand, carbons for EDLCs can be tolerant to high scan rates and long cycling but show specific capacities generally lower than 400 F/g in aqueous electrolytes or 200 F/g in organic electrolytes. Mxenes or related composites have demonstrated high volumetric capacities of above 1000 F/cm^3. Probably due to their high stability and low cost, most commercialized electrode materials are carbon materials [8,9].

Several strategies, including optimization of electrolytes and construction of asymmetric capacitors or Li-ion capacitors, have been investigated to further improve the performance [28–30]. In the pursuit, a fundamental understanding of the electrochemical interface at the nanoscale and the behavior of ions in pores is critical. Because of the versatile structure of electrode materials, the puzzles may include but not be limited to the following aspects: how are the charges effectively stored at the electrolyte/electrode interface? How does the electrical double layer form and is organized in the limited space of sinuous pores? How are the electrolyte ions arranged in the pores? What are the specific factors determining the ionic dynamic through pores?

Surely the answers to the above-mentioned questions would provide guidance for developing better electrode materials and advancing the electrochemistry for supercapacitors. In the typical evaluations of electrodes, however, off-line current and voltage measurements yield an "integrated capacity", which may not reflect the exact and instantaneous state during charging or discharging. With the improvement of *in-situ* characterization techniques, researchers shall have chances to monitor the behavior of electrolytes or the change of electrodes during the electrochemical process [31]. Furthermore, combining the *in-situ* characterizations and theoretical simulations with electrochemical characterizations allows one to develop the descriptors for the charge storage process and thus to supplement a view for the construction of better supercapacitors.

In this article, we will briefly review the working principles of supercapacitors and the advances on charge storage mechanisms of supercapacitors using *in-situ* techniques such as infrared (IR) spectroscopy, small angle X-ray/neutron scattering (SAXS/SANS), electrochemical quartz crystal microbalance (EQCM) and nuclear magnetic resonance (NMR) spectroscopy. Perspectives and remarks on the future research are discussed in the final section.

2. Structure and working principle of supercapacitors

A typical supercapacitor consists of two electrodes separated by an ion-permeable separator (*e.g.*, cardboard, ceramic, glass, plastic or paper) and electrolyte that ionically connects two electrodes. On the electrodes, the charges are stored either in a Helmholtz double layer at the electrode–electrolyte interface or via redox reactions between electrolyte and electrode. The former leads to EDLCs and the latter to pseudocapacitors.

2.1. EDLCs

In an EDLC, positive and negative ions in the electrolyte move towards electrodes driven by an electric field and form a charged layer near the surface of the electrode. As shown in Fig. 1(a), this

Table 1
Typical electrode materials and performances of supercapacitors reported in literatures. Except for in Ref. [24], the specific capacitance is normalized to single electrode based on the two-electrode devices.

Type of electrode material	Electrode materials	Synthetic method	Testing method	Electrolyte	Scan rate	V (V)	C_v (F cm^{-3})	C_g (F g^{-1})	Cycle lifetime (retention)	Ref.
Carbon materials	a-MEGO	KOH activation	two-electrode	1 M BMIM BF_4/AN	5.7 A g^{-1}	3.5	/	166	10,000 (97%)	[10]
	EM-CCGS	self-assembly	two-electrode	1 M H_2SO_4	0.1 A g^{-1}	1.0	255	191.7	50,000	[11]
	EM-CCGS	self-assembly	two-electrode	1 M BMIM BF_4/AN	0.1 A g^{-1}	3.5	261	196	5000	[11]
	PAN-*b*-PMMA-CFs	block copolymer microphase separation	two-electrode	6 M KOH	1.0 A g^{-1}	0.8	/	360	10,000	[12]
	CNT/GP	microwave plasma chemical vapor deposition	three-electrode	1 M H_2SO_4	1 mA cm^{-2}	1.0	/	500	10,000 (95%)	[13]
	Activated carbon	KOH activation	two-electrode	6 M KOH	0.5 A g^{-1}	1.0	/	427	5000 (94%)	[14]
	Activated carbon	KOH activation	three-electrode	6 M KOH	0.1 A g^{-1}	1.0	550	519	/	[15]
	Activated carbon	KOH activation	two-electrode	6 M KOH	0.1 A g^{-1}	1.0	369	369	20,000 (100%)	[15]
Metal oxides	Co_3O_4	high temperature calcination	three-electrode	1 M KOH	1.0 A g^{-1}	0.55	/	770	5000 (82%)	[5]
	Ag/NiO	hydrothermal	two-electrode	2 M KOH	2.5 A g^{-1}	0.5	/	204	4000 (96%)	[7]
	Mn_3O_4	high temperature calcination	three-electrode	0.6 M KOH	5 mV s^{-1}	0.6	/	125	2100 (80%)	[16]
	RuO_2/graphene	combining sol–gel and low-temperature annealing processes	three-electrode	1 M H_2SO_4	1 mV s^{-1}	1.0	/	570	1000 (98.2%)	[17]
	MnO_2/graphene	solution-phase assembly	two-electrode	1 M Na_2SO_4	0.5 A g^{-1}	2.0	/	31.0	1000 (98%)	[18]
	GO/MnO_2	self-assembly	three-electrode	1 M Na_2SO_4	0.2 A g^{-1}	1.0	/	197.2	1000 (84.1%)	[19]
	MnO_2/graphene	microwave irradiation	three-electrode	1 M Na_2SO_4	1 mV s^{-1}	1.0	/	310	15,000 (95.4%)	[20]
	CNT/MnO_2	self-assembly	three-electrode	1 M Na_2SO_4	500 mV s^{-1}	1.0	/	522	500 (94.6%)	[21]
Conductive polymers	PPy	KOH activation	two-electrode	$EMIMBF_4$	0.1 A g^{-1}	4.6	/	290	10,000 (108%)	[22]
	PANI	KOH activation	three-electrode	2 M KOH	1.0 mV s^{-1}	1.0	/	455	2000 (94.6%)	[23]
	PANI/RGO	self-assembly	two-electrode	PVA/H_2SO_4	0.08 A g^{-1}	0.8	148	112	17,000) (95%)	[24]
MXene	$Ti_3C_2T_x$ films	Ti_3AlC_2 dissolving LiF in 6 M HCl	three-electrode	1 M H_2SO_4	2 mV s^{-1}	0.6	900	245	10,000 (100%)	[25]
	$Ti_3C_2T_x$/CNT composite paper	vacuum-assisted filtration	three-electrode	1 M $MgSO_4$	2 mV s^{-1}	1.0	390	/	1000 (100%)	[26]
	$Ti_3C_2T_x$/rGO	electrostatic self-assembly	three-electrode	3 M H_2SO_4	2 mV s^{-1}	1.0	1040	335.4	20,000 (100%)	[27]

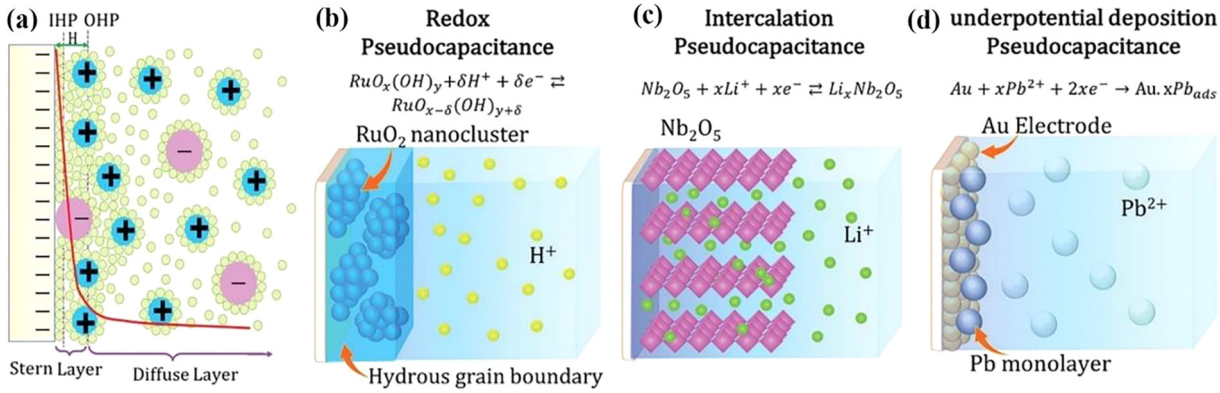

Fig. 1. Schematics of charge-storage mechanisms for (a) EDLC and (b–d) different types of pseudocapacitive electrodes: (b) Redox pseudocapacitor, (c) ion intercalation pseudocapacitor and (d) underpotential deposition. Adapted with permission from [37], Copyright 2019, the Royal Society of Chemistry.

charged layer typically consists of an inner tight layer (Stern layer) and an external diffusion layer namely electric double layer [32]. The tight layer is further composed of an inner Helmholtz layer (IHP) including solvent and characteristically adsorbed ions and an outer Helmholtz layer (OHP) mainly with solvated ions. The interaction between solvated ions and charged electrodes is a long-range electrostatic force and less dependent on the chemical properties of ions, so the ions in OHP are called non-characteristically adsorbed ions. Upon a thermal disturbance, the non-characteristically adsorbed ions may diffuse into the diffusion layer from OHP to bulk solution. During the charging, electrons are transferred to the negative electrode from the positive electrode through the external circuit. In the meantime, cations in the electrolyte tend to move to the negative electrode and anions to the positive electrode for compensation. In the discharging the ions tend to (but not always) go to the opposite electrodes. Roughly the capacity of EDLC can be estimated with Eq. (1) [31–33]:

$$C=\frac{\hat{I}u_r\hat{I}u_0}{d}A, \quad (1)$$

where ε_r is the relative permittivity of the electrolyte used, ε_0 the permittivity of vacuum, A the effective surface area of the electrode material which is accessible to the electrolyte ions, and d the effective charge separation distance in the EDLC, *i.e.*, the Debye length.

2.2. Pseudocapacitors

Pseudocapacitors rely on fast and reversible faradaic redox reactions to store charges. The capacitance in a pseudocapacitive electrode may be attributed to: (1) Redox pseudocapacitance, in which reductive species are absorbed onto the surface or near the surface of oxidative electrodes in a Faradaic system (*e.g.*, RuO_2 or MnO_2, as well as some conducting polymers, as shown in Fig. 1b) [32,34,35]. The surface redox dominated pseudocapacitive behaves just like EDLC, demonstrating linear galvanic charge/discharge (GCD) curves and nearly rectangular cyclic voltammetry (CV) curves; (2) intercalation pseudocapacitance, in which the reversible intercalation/de-intercalation of cations (Na^+, K^+, Li^+, H^+, *etc.*) into the electrode materials is involved. It is worth noting that a material phase change does not necessarily occur in the intercalation-involved pseudocapacitor (*e.g.*, Nb_2O_5, as shown in Fig. 1c) [28,32,36]; and (3) underpotential deposition-based pseudocapacitance, in which ions deposit on a metal-electrolyte interface at potentials positive to their reversible redox potential (*e.g.*, H^+ on Pt or Pd^{2+} on Au, shown in Fig. 1d) [32,37,38]. One shall note that some pseudocapacitors share similar features with batteries while in most situations the pseudocapacitive process occurs on or nearby the surface of electrodes to achieve a high power capacity.

3. *In-situ* characterization techniques

A few *in-situ* techniques have been used in Li-ion batteries to obtain insight on the evolution of electrodes and solid-electrolyte interphase (SEI), information on side reactions and ion transport properties [39–41]. Compared to batteries, however, the energy storage in supercapacitors is more surface sensitive, while with less phase or volume changes of electrodes, nor the formation of SEI [42,43]. Hence, some techniques used to detect the structural evolution of bulk electrodes, *e.g.*, scanning electron microscopy (SEM), transmission electron microscopy (TEM) and X-ray diffraction (XRD), may not provide very useful information for electrodes of supercapacitors. Typically very fast kinetics of the surface process in supercapacitors also restricts the applications of some techniques such as X-ray photoelectron spectroscopy (XPS), X-ray absorption (XAS) and Raman spectroscopy, as these techniques usually need long sampling time or harsh testing environments.

These factors have restricted the applications of the *in-situ* techniques to supercapacitors. Table 2 summarizes several commonly used *in-situ* techniques for EDLC electrodes. Among them, *in-situ* IR spectroscopy is used to detect molecular vibrations and rotational energy levels, providing the following information: (1) Chemical nature (*e.g.*, bonding and orientation) of adsorbates, solution species and production species in the thin layer of electrolyte involved in the electrochemical reactions and (2) some short-life intermediates in the reactions based on time-resolved spectroscopy, revealing the reaction kinetics on electrodes [44–46]. SAXS and SANS can be used to obtain the real-time information of ion distribution and species of solution when a cyclic voltage is applied [47,48]. Using EQCM, the mass change of electrode surface related to Faraday's law can be quantitatively calculated to understand the behavior of solvent ions on the electrode surface, providing information on the reaction process of the electrode surface from a new perspective [9,35,49]. The changes in NMR frequency and intensity reflect difference in the molecular structure and chemical environment, giving hints about the ion type and number on the electrode surface or near the surface [50–52]. It is worth noting that the quick yet complicated redox reactions on electrodes would bring more challenges in the *in-situ* studies of pseudocapacitors, thus the ion adsorption and diffusion studies have been focused mainly on EDLC electrodes. In addition, *in-situ* measurements may raise other requirements for the cell assembly of supercapacitors, depending on the technique utilized.

Table 2
Summary of *in-situ* characterizations typically used for supercapacitor electrodes.

In-situ technique	Information to obtain	Advantages	Disadvantages	Ref.
IR	Intensity and wavelength of absorption peak	Variation of the absorption intensity of anions and cations can be separately obtained in real time	It is difficult to measure the ion changes in the pores	[31,53,54]
SAXS/SANS	Scattering intensity of X-ray/neutron at different scattering angles	Information of ion adsorption in different channels can be observed; Scattering intensity variation (the difference in electron density/nucleus of anion and cation) may explain the energy storage mechanism	It is difficult to distinguish the type and number of ions only based on scattering	[47,55]
EQCM	Mass of electrode from the vibration frequency of quartz crystal	Combining mass change with the valence state of an adsorbed anion or cation can be used to quantitatively estimate the adsorption species; Monitoring adsorbed ion mass change in electrolyte with/without solvent can detect the desolvation process in restricted space	It is difficult to justify the attribution of the mass change in inorganic, solvent-containing organic electrolyte (anion, cation or solvent molecules); It is not suitable for viscoelastic samples and pseudocapacitance reaction systems	[56,57]
NMR	Nuclear magnetic resonance frequency and intensity in local environments	Ion concentration inside and outside the pores can be measured separately; Changes of ions number in different environments can be quantitatively studied; Variation of the width of nuclear magnetic peak helps to understand the ionic dynamics information	The resolution is limited and nuclear magnetic active elements are needed	[58–60]

3.1. *In-situ* IR spectroscopy

For *in-situ* IR, one challenge is how to make sure the incident light precisely reaches the electrode/electrolyte interface or the desired regions [31]. Among various configurations, experiments using *in-situ* attenuation total reflection (ATR) IR spectroscopy have shown powerful to investigate the electrochemical interface, as ATR minimizes the IR absorption of bulk electrolyte. Normally, two modes, internal and external reflections, are utilized in ATR IR, as shown in Fig. 2(a) [61]. In the internal reflection electrolytic cell (left scheme in Fig. 2a), an infrared window plate with high refractive index (Ge, Si, ZnSe, etc) is plated with a layer of thin metallic film (working electrode) with a thickness of dozens of nanometers. The total reflection occurs at the interface between

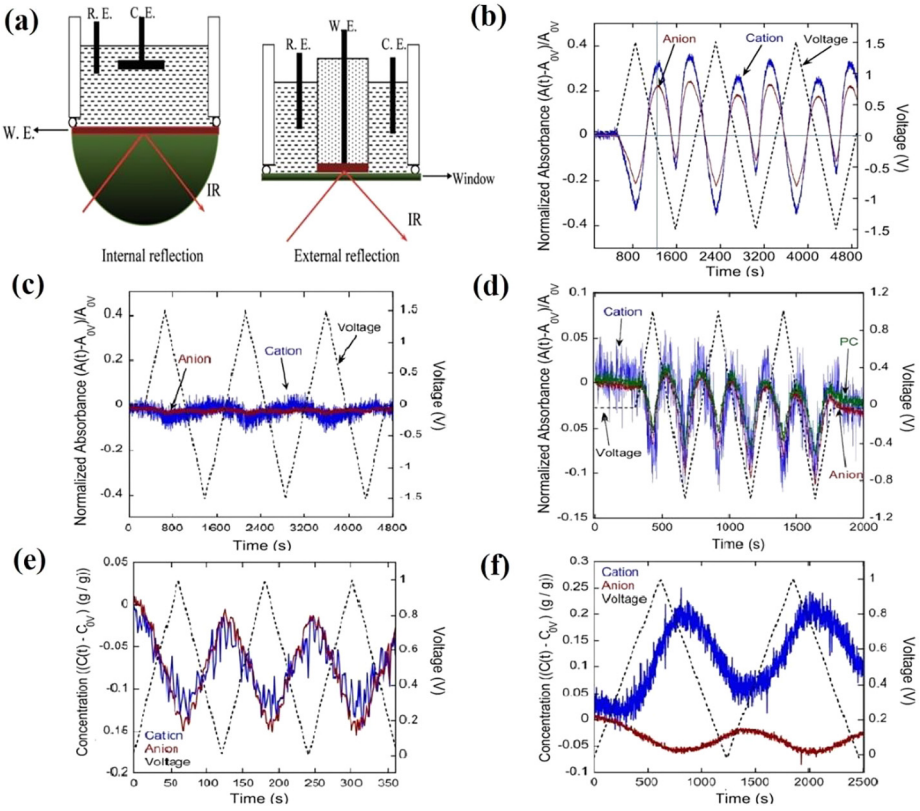

Fig. 2. (a) Schematic of *in-situ* IR with internal and external reflection configurations. Adapted with permission from [61], Copyright 2012, American Association for the Advancement of Science. Normalized infrared absorbance of EMIM-TFSI as a function of time in three CV cycles from −1.5 to +1.5 V at a scan rate of 5 mV/s for (b) CDC and (c) OLC. (d) Normalized infrared absorbance of EMIM-TFSI and PC in a 50% EMIM-TFSI/PC concentration as a function of time in three CV cycles from −1 to +1 V. Adapted with permission from [62], Copyright 2013, American Association for the Advancement of Science. Initialized time-resolved concentration (unit $g_{EMIM-TFSI}/g_{electrode}$) of $EMIM^+$ and $TFSI^-$ in neat EMIM-TFSI electrolyte in three CV cycles from 0 to 1 V in electrodes for (e) NCNFs and (f) KOH-activated NCNFs. Adapted with permission from [63], Copyright 2014, American Association for the Advancement of Science.

the metal film and the window, but the implicit wave of infrared light still reaches the solution interface through the metal film and attenuates exponentially. The IR can penetrate in a depth of about 0.4–1 m into the working electrode (depending on the wavelength) [46], well covering the adsorbed species [62]. In the external reflection (right scheme in Fig. 2a), the working electrode is placed in close contact with the light guiding prism; the thin liquid layer (1–10 μm) between electrode and prism provides the path for IR. As the layer is thin enough for the solvent, the reflected light can be absorbed by species. Hence, this configuration can be used for a wide range of electrode materials and allows to simultaneously determine the species in the electrolyte and those absorbed on the electrode [54]. In ATR IR, excess amount of electrolyte or bubbles shall be avoided to cause the undesired absorption.

The specific surface area (SSA) and pore distribution of carbon electrode materials are key factors affecting the electrochemical energy storage. By capturing the signal of thin liquid layer in the external *in-situ* reflection IR, the ionic dynamics in electrodes of onion-like carbons (OLCs, with small amount of holes) and carbide-derived carbons (CDCs, with a highly porous structure) in ionic liquid (IL, 1-ethyl-3-methylimidazolium bis(trifluoromethyl sulfonyl)imide, EMIM-TFSI) electrode has been investigated [62]. As shown in Fig. 2(b), the IR absorbance intensity of both cation ($EMIM^+$) and anion ($TFSI^-$) increases when the voltage decreases from +1.5 V and reaches the maximum at 0 V for CDC; the absorbance intensity decreases in the reversed scans (0 to −1.5 V). The behavior suggests a process of co-ion adsorption. The cyclic absorbance also clearly shows that the ions in pure IL electrolyte enter or escape from the CDC in charging or discharging. In contrast, the IR absorption of the same ions remains nearly unchanged for OLC under the same conditions (Fig. 2c), suggesting that the ions are located close to the surface of OLC with fast ion kinetics in charging or discharging. This may explain why CDC has the higher specific capacitance, while OLC has an excellent power, providing a guidance for the fine balance between porous structure and short ion diffusion distance. The effect of electrolyte concentration is also investigated by *in-situ* IR. For EMIM-TFSI diluted in propylene carbonate (PC) with a mass concentration of 10%, a constant decease in the absorbance of PC has been observed with time, possibly due to the evaporation of PC or the trap of PC by the carbon particles [62]. For a 50% EMIM-TFSI/PC concentration, the PC molecules enter or exit from the pores with the IL ions, as shown in Fig. 2(d), due to the strong IL-PC solvation interaction. The result indicates that the interaction between solvent molecules and ions can significantly affect the electrochemical process. The results agree with the work of Gebbie et al. in which PC does not enter the pores in a lower concentration electrolyte (EMIM-TFSI/PC), while the opposite phenomenon was observed for the higher concentration when the CDC electrode was used [64].

Meanwhile, the ionic behavior is sensitive to the surface properties of electrode materials [47,65]. In the external *in-situ* reflection IR, an experiment with nanoporous carbon nanofibers (NCNFs) or potassium hydroxide (KOH)-activated NCNFs revealed the different ionic dynamics when oxygen-containing functional groups were introduced [63]. BET (Brunauer-Emmett-Teller) and XPS analyses suggest that KOH activation does not obviously change the average pore size of NCNFs but increases the oxygen content from 2.9% to 4.9%. As shown in Fig. 2(e), for NCNF electrode, the absorption of both $EMIM^+$ and $TFSI^-$ decreases when the voltage is scanned from 0 to 1 V, indicating that the cations and anions simultaneously enter the nanopores of NCNFs together due to the strong Columbic interaction between ions. In contrast, the cation absorption increases while the anion absorption decreases in the charging of KOH-activated NCNF electrodes, as shown in Fig. 2(f). The difference suggests that the oxygen functional groups play roles in the kinetics of ions. It is presumed the oxygen groups induce negative charges to the carbon surface which makes the pores more favorable to $EMIM^+$ under the open circuit potential. Thus, in the positively charging the cations are expelled from the nanopores but anions adsorbed into the nanopores [63]. By modifying electrode materials, such as with surface functionalization, the charge storage process and the following electrochemical performance could be optimized.

3.2. In-situ scattering

Small-angle scattering refers to the scattering within an angle range of 2–5°. SAXS detects the fluctuation of electron density of target materials with a particle size of 1–100 nm, while SANS reflects the density difference of neutrons [47,55]. In contrast to SAXS, SANS can accurately determine the position of light and heavy atoms in the structure. Fig. 3(a and b) schematically show the experimental setups of SAXS and SANS, respectively, in which the small-angle scattering signal is recorded using a 2D position sensitive X-ray/neutron detector and the transmission signal recorded using an X-ray/neutron sensitive photodiode [66,69]. In the *in-situ* testing with SAXS/SANS, coin cells with windows has been widely used to contain a sandwiched configuration of platinum current collector, working electrode/separator/counter electrode, and another platinum current collector in a polyether ether ketone (PEEK) housing [66,70]. Thin or porous current collector with a low load mass of electrode material is necessary to assure the transmission of X-ray or neutrons.

SAXS has been used to evaluate the behavior of adsorbed molecules in nano and sub-nano channels. For example, Prehal et al. investigated the spatial arrangement of various electrolytes (1 M CsCl, KCl or NaCl) in an activated carbon (AC, YP-80) with SAXS [66]. As shown in Fig. 3(c and d), the mapping of scattering intensity versus scattering vector modulus *Q*, can be obtained under the scanning voltage applied. The mapping can be categorized into two main regions: Q-A ($Q < 5\ nm^{-1}$) and Q-B ($Q > 5\ nm^{-1}$) with different intensity distributions. With the power law decay of the intensity, the SAXS intensity of Q-A region is attributed to the large porous structure in the AC particles; while Q-B is dominated by the small pores, as well as the electrolyte in pores [48,55]. In 1 M CsCl, the change of the scattering is dominated by the cation concentration due to the higher number of electrons in Cs^+ than in Cl^-. As shown in Fig. 3(c), the scattering intensity in Q-B region increases (with the color changing from red to white) in the scan from 0 to −1 V, suggesting that the Cs^+ adsorption occurs in discharging. The scattering intensity decreases (with the color changing from red to blue) in the reversed scans (from 0 to 1 V), suggesting that the Cs ion desorption occurs in charging process. This behavior means a process of count-ion desorption for AC in 1 M CsCl. In contrast, with the same electron number, the scattering intensity of K^+ and Cl^- in Q-B region is hardly changed neither from 0 to 1 V (almost blue) nor from 0 to −1 V (mostly yellow), as shown in Fig. 3(d). A reversed result was found for 1 M NaCl in the Q-B region when compared to that situation for 1 M CsCl, due to the fact that the number of electrons in the Na^+ ion is less than that in the Cl^- ion [66].

In-situ SANS has also been used to investigate the ion adsorption process in micropores under different voltages. Generally, ^1H has the high neutron scattering cross-section but ^{10}B (20% in nature) can absorb neutrons very well [71,72]. For TEATFB (tetraethylammonium tetrafluoroborate, $N(C_2H_5)_4BF_4$) electrolyte, the higher concentration of $N(C_2H_5)_4^+$ in the pore means the increase in neutron scattering intensity, while the neutron scattering intensity is attenuated with the higher presence of BF_4^- in pores [68]. As shown in Fig. 3(e), the lower scattering intensity at +2 V found in activated carbon fabric (ACF) for TEATFB in deuterated acetonitrile (d-AN) can be attributed to the process

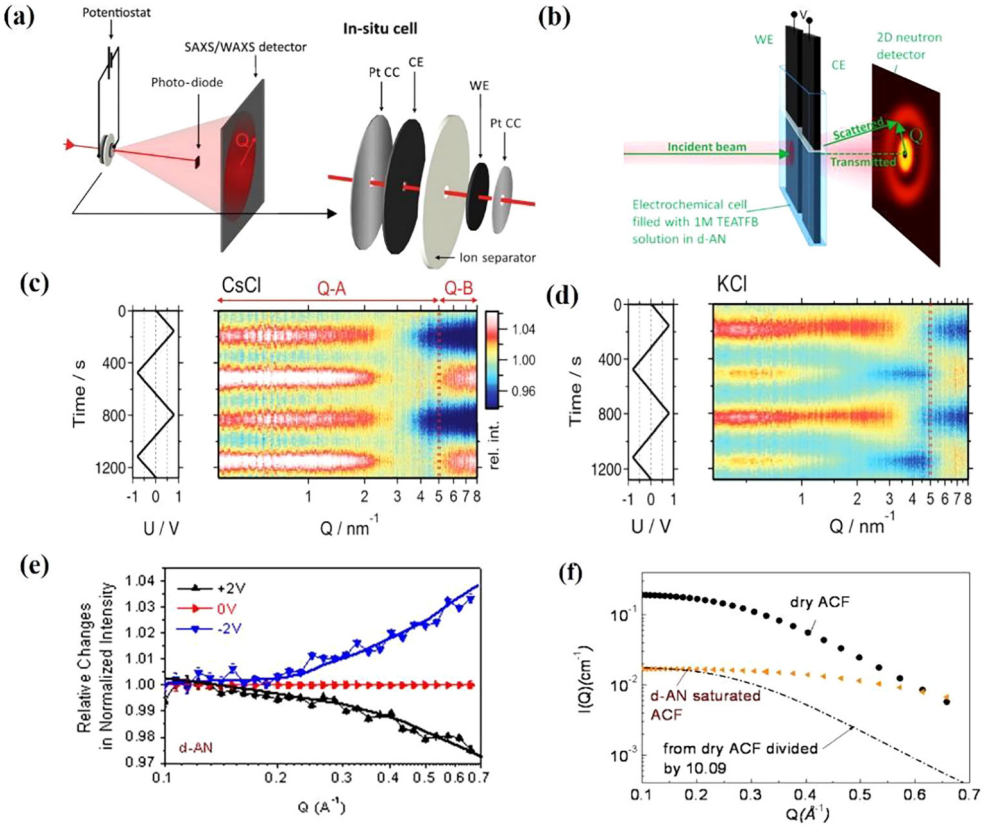

Fig. 3. Schematics of (a) SXAS setup. Adapted with permission from [66], Copyright 2015, the Royal Society of Chemistry, and (b) SANS setup. Adapted with permission from [67], Copyright 2014, American Association for the Advancement of Science. SAXS intensity (color coded scale) normalized to the intensity at 0 V as a function of time and the scattering vector length (Q) in 1 M (c) CsCl and (d) KCl. Left rows show the applied voltage signal as a function of time. Adapted with permission from [66]. Copyright 2015, the Royal Society of Chemistry. (e) Relative changes in the intensity of the normalized SANS profiles in 1 M TEATFB/d-AN electrolyte under various potentials. (f) SANS intensity on dry ACF electrodes and ACF immersed into d-AN. Adapted with permission from [68], Copyright 2014, American Association for the Advancement of Science.

that $N(C_2H_5)_4^+$ are replaced with BF_4^- and solvent molecules. The higher scattering intensity at −2 V may arise from the adsorption of H-containing $N(C_2H_5)_4^+$ in the pores. It should be noted that the exclusion of BF_4^- from the pores also contributes to the increase in the scattering intensity, which may account for the larger relative change in normalized intensity in $Q > 0.2$ Å^{-1} at negative voltage, suggesting that the micropores exhibit higher initial concentration of naturally adsorbed BF_4^-, and the wetting behavior of ions can affect the charge storage. Furthermore, the wetting of d-AN in micropores was also studied by SANS. Due to the smaller scattering contrast between carbon and deuterated solvents than that between carbon and air (the scattering intensity is proportional to the square of scattering difference, $(\Delta I)^2 = (I_c - I_{el})^2$), the scattering intensity ($I(Q)$) of ACF in d-AN is lower than that in dry ACF (Fig. 3f). In $Q < 0.2$ Å^{-1}, two vertical downshift scattering curves for dry ACF and ACF infiltrated with d-AN suggest that d-AN has completely and uniformly wetted all large pores. However, the gradual divergence of the two curves ($Q > 0.2$ Å^{-1}) shows that a significant portion of the sub-nanometer pores is not completely filled with d-AN [68].

3.3. Electrochemical quartz crystal microbalance (EQCM)

Electrochemical quartz crystal microbalance is a device that combines inverse piezoelectric sensors with electrochemical devices to convert the frequency change (Δf) to mass change (Δm) on electrodes, as shown in Fig. 4(a). The conversion follows the Sauerbrey equation (Eq. (2)) [56,57]:

$$\Delta m = -\frac{A\sqrt{u_q p_q}}{2f_0^2}\Delta f = -C_f \Delta f \quad (2)$$

where f_0 is the fundamental frequency, A is the area of active surface, μ_q is shear modulus of quartz (2.947×10^{11} g cm^{-1} s^{-2}), ρ_q is the density of quartz crystal (2.65 g cm^{-3}), and C_f is the sensitivity factor. The model in principle is only suitable to the situation in which the adsorption film is rigid and homogeneous without lateral sliding. It is believed that EDLC consists of rigid adsorption; but for pseudocapacitance, there is a controversy whether the Sauerbrey equation is proper to calculate the mass changes of an electrode in Faraday reaction [57]. To maintain the high detection sensitivity (~10^{-9} g), some strict requirements on the sample preparation have to be considered in EQCM [56,57]. Among them, a ultrathin and homogeneous sample coated on the quartz sensor is very important to enable the high fundamental resonance frequency without much damping.

Levi et al. have made pioneering work on using EQCM as a mass probe to measure the ion adsorption and desorption in porous carbon electrode. Fig. 4(b) shows CV curves at different scan rates and the change of frequency and resonance peak width for a TiC-CDC electrode in 0.1 M KCl [73]. In EQCM, the damping of oscillation is expressed with dissipation factor $\Delta D = \Delta W/f_o$, which is related to the viscosity and elastic modulus of the adsorption layer on the quartz crystal, indicating the internal energy consumption of the sensor system [56]. The nearly unchanged ΔW across the potential range means this adsorption can be roughly considered as a rigid model. The potential for the frequency maximum (pfm) is close to the potential of zero charge (pzc) in CV and the lower

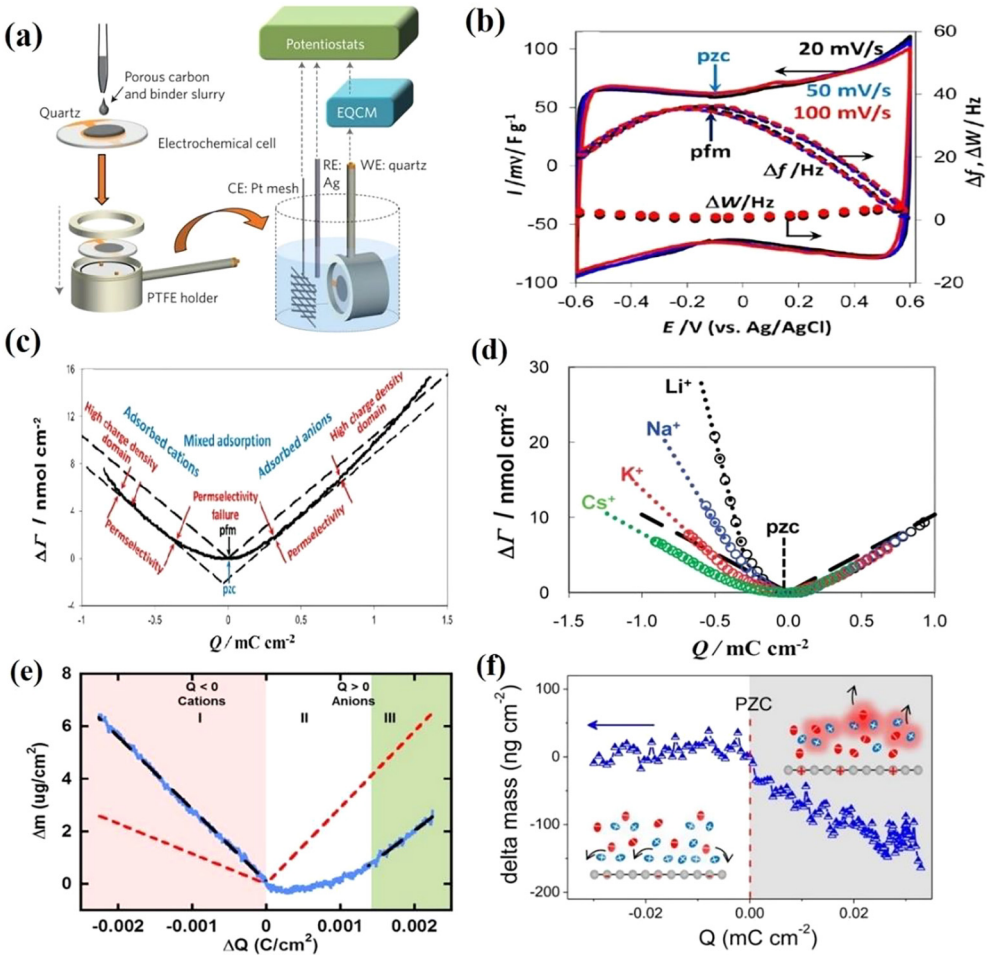

Fig. 4. (a) Schematic of electrochemical quartz crystal microbalance; (b) CVs, frequency shifts (Δf) and resonance peak width variations (ΔW) vs. potential for TiC-CDC carbon electrode in 0.1 M KCl at different scan rates. (c) $\Delta\Gamma$ vs. Q curve (solid line). The dashed lines are the Faradaic straight lines for the adsorption of K^+ and Cl^-. Adapted with permission from [73], Copyright 2013, American Association for the Advancement of Science. (d) $\Delta\Gamma$ vs. Q plots of carbon electrode in 0.1 M alkaline metal chlorides. Adapted with permission from [74], Copyright 2011, American Association for the Advancement of Science. (e) Electrode mass change vs. charge during the polarization of CDC-1 nm in 2 M EMI-TFSI/AN. Blue solid line is the measured mass change; red line indicates the theoretical mass change of neat ions calculated from Faraday's law. The black dashed line shows the linear fitting of measured mass change. Adapted with permission from [49], Copyright 2014, American Association for the Advancement of Science. (f) Electrode mass change vs charge during the polarization of SLG on gold substrate in EMI-TFSI recorded at 50 mV s^{-1}. Inset: scheme showing the ion fluxes on SLG surface during polarization. Free EMI^+ cations are in blue; free $TFSI^-$ anions are in red. Adapted with permission from [75], Copyright 2019, American Association for the Advancement of Science.

Δf indicates the increase of Δm which may be related to ion adsorption at potentials other than pzc. Fig. 4(c) plots the population change ($\Delta\Gamma$) of cations (at $Q < 0$) and anions (at $Q > 0$), which is calculated using the atomic weight (M) of the bare ions: $\Delta\Gamma = \Delta m/M$. Assuming a 100% counterion adsorption efficiency, $\Delta\Gamma$ can also be calculated with the Faraday's law. By comparing experimental and theoretical curves, three different regions may be distinguished: (1) For moderate charge densities, the slope of experimental plot is equal to that of the Faradaic straight line, signifying that EDLC contains counterions only; (2) near the pzc, a considerably diminished slope indicates the simultaneous presence of counter- and co-ions in EDLC; (3) for high charge densities, a gradually increased slope may suggest the adsorption of desolvated ions in sub-nanometer pores, thus increasing the total mass of adsorbed ions due to the higher numbers of ions [73].

Solvation of different alkali metal ions in AC materials has been investigated using EQCM [73,74,76], as shown in Fig. 4(d). Compared to bare alkali metal ions acquired with the Faraday's law (black line), Li^+ and Na^+ ions show higher slopes, indicating the cations have higher effective mass than expected. In contrast, K^+ and Cs^+ ions demonstrate slopes close to the Faradaic straight line, suggesting that the effective ions mass is close to the mass of the bare ions. Thus, the highly solvated cosmotropic ions in the bulk solution, are desolvated when entering sub-nanometer pores. Tsai et al. performed EQCM to characterize ion adsorption in CDC with average pore sizes of 1 and 0.65 nm, respectively [49]. They found that it is more difficult for EMI^+ and $TFSI^-$ ions in AN to access 0.65 nm channel than 1 nm channel, and ions try to adapt to smaller channels by reducing the degree of solvation (*e.g.*, by adjusting the solvation index from 3–4 to 1–2). Different electrochemical processes based on the charge stored in the electrode has been determined, as shown in Fig. 4(e). In region I, for negative charge ($\Delta Q < 0$), the measured mass change is higher than that predicted for bare ion adsorption, suggesting the additional mass from solvent molecules. In positive charge ($\Delta Q > 0$), the slope of the plot is always less than the theoretical line and it is linear only at higher charge in region III ($Q > 0.4$ mC/cm^2). Such a behavior can be explained by the existence of a cation–anion mixing zone, *i.e.*, the ion exchange. In contrast to the porous structure, two-dimensional carbons such as graphene may provide a good platform for the study of adsorption and desorption behavior of ions at the carbon-electrolyte interface. Ye et al. used EQCM to charac-

terize the ion fluxes and adsorption on single layer graphene (SLG) in neat EMI-TFSI electrolyte [75]. As shown in Fig. 4(f), the electrode mass has no significant change from pzc to more negative charges, indicating that the applied potential cannot bring more species onto SLG surface, thus very likely, implying an ion reorganization in the compact layer. However, the electrode weight decreases linearly with the for $Q \geq 0$, indicating a charging mechanism of positively charged-ion-species desorption. This result is totally different from the situation in porous carbons, highlighting the role of electrostatics correlations on ionic kinetics on an open carbon interface.

3.4. In-situ nuclear magnetic resonance (NMR) spectroscopy

NMR spectroscopy is a promising tool for detecting the structure and dynamics of the electrode–electrolyte interface in supercapacitors. The approach has been used for Li-ion batteries (LIB, Fig. 5a). For supercapacitor study (Fig. 5b), a 'shifted' bag cell

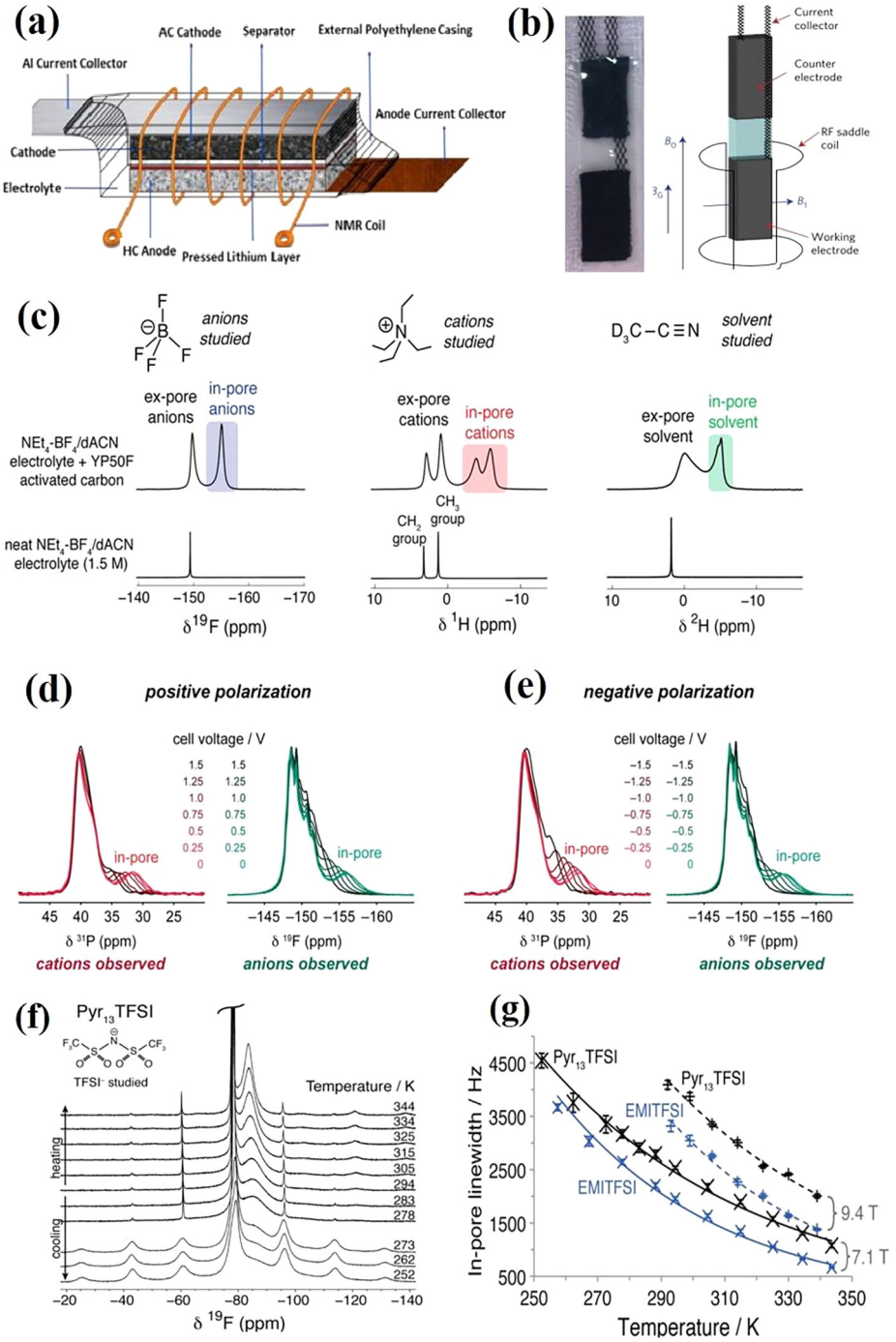

Fig. 5. (a) Schematic of an assembled LIC pouch cell for *in-situ* NMR; Adapted with permission from [72], Copyright 2016, American Association for the Advancement of Science. (b) A supercapacitor cell design for *in-situ* NMR. (c) NMR measurements of YP50F activated carbon soaked in NEt_4-BF_4/dACN. Adapted with permission from [80], Copyright 2016, American Association for the Advancement of Science. (d) ^{31}P and (e) ^{19}F NMR spectra of a supercapacitor containing PEt_4-BF_4/ACN electrolyte. (f) ^{19}F NMR (7.1 T) spectra of YP50F film soaked in $Pyr_{13}TFSI$ at different temperatures. (g) Measured in-pore line widths (full width at half-maximum). Adapted with permission from [81], Copyright 2015, American Association for the Advancement of Science.

design is constructed from flat pieces of electrode films pressed onto a mesh current collector. A small strip of porous polymer membrane separator is placed between two electrodes and the whole assembly is heat-sealed inside a plastic bag. Electrolyte is added to the supercapacitor using a micro syringe before the final seal. In this device, an excellent sealing shall be ensured to reduce the volatilization of the electrolyte and ohmic resistance (circuit contact resistance and solution resistance). The success of NMR method stems from its ability to distinguish the ions species confined in carbon nanopores (intrapore ions) and those located between carbon particles and bulk electrolytes (extrapore ions) [52,77]. When an external magnetic field was applied on sp^2 carbon, the ring current induces electron circulation within the delocalized π-orbitals, resulting in chemical shielding effect, thus the chemical shift of the adsorption element is moving to the lower chemical shift. For YP50F soaked in the electrolyte NEt_4-BF_4 (tetraethylammoniumtetrafluoroborate) in AN (Fig. 5c), ions and solvent molecules inside/outside the pores give rise to peaks which are distinct to those from bulk electrolyte; the chemical shift of the atomic nuclei adsorbed on the surface of carbon is lower relative to those of the free extrapore nuclei. So the change of chemical shift is closely related to the chemical environment of the nucleus [78,79].

In-situ NMR has been utilized to track the ion movement trajectory in porous electrodes at different operating voltages in real time. Griffin et al. studied the ^{19}F and ^{31}P NMR spectra in PEt_4-BF_4/AN (tetraethylphosphonium tetrafluoroborate) electrolyte recorded at different charging states [80]. As the voltage value increases, the higher chemical shift of cation and anion in ^{19}F NMR or ^{31}P NMR indicates the stronger Coulomb force due to the reduction of distance between ions and electrode surface (Fig. 5d and e). Meanwhile, the resonance intensity of BF_4^- in positive polarization (Fig. 5d) or PEt_4^+ in negative polarization (Fig. 5e) increases with the voltage, indicating the gradually increased number of adsorbed counterions. *In-situ* NMR may provide guidance for the development of new electrolytes by observing the kinetic behavior of electrolyte ions in porous electrode materials. Forse et al. recorded in- and ex-pore resonance line width change of ^{19}F at different temperatures to evaluate the movement of ions in YP50F [81]. As shown in Fig. 5(f), the ex-pore resonance (−78.3 ppm) does not show any significant changes in line width, while the in-pore (−84.9 ppm) line width steadily decreases as the temperature increases in Pyr_{13}TFSI (1-methyl-1-propylpyrrolidinium bis(trifluoromethanesulfonyl)imide). The NMR spectra of EMITFSI show similar changes of the in-pore line width with the temperature. The in-pore line width mainly arises from two aspects: Dipole-dipole interaction and ion adsorption sites in the carbon micropores [82,83]. In the former case, the line width is not sensitive to the magnetic field strength [60,83]. However, compared to the results measured at a magnetic field of 7.1 T, the line widths of Pyr_{13}TFSI and EMITFSI show a significant increase at a magnetic field of 9.4 T in the temperature range studied (250–350 K) (Fig. 5g), indicating the contribution from different adsorption sites. In the absence of any motion, each ion contributes separately to the spectrum and the line shape represents the weighted distribution of the different chemical shifts. The diffusion (or chemical exchange) of ions between different sites leads to line shape perturbations. When the rate of diffusive motion exceeds the frequency width of the distribution of chemical shifts, a single coalesced resonance is observed which is narrower than the overall distribution of shifts [51,82]. Thus, the in-pore line width gives a measure of how quickly the ions diffuse through the carbon pores; the faster the diffusion is, the narrower the intrapore resonance. As shown in Fig. 5(f and g), the ions diffuse more quickly between different sites with the temperature increases. ^{19}F in-pore line width is smaller for EMITFSI than Pyr_{13}TFSI over the temperature range of interest, suggesting the faster diffusion of in-pore anions in EMITFSI than in Pyr_{13}TFSI (Fig. 5g) [82]. By comparing ^{19}F and ^{1}H spectra with those obtained without solvent, we can see that the line widths of the in-pore resonances are dramatically reduced in AN. Thus, the addition of AN solvent dramatically increases the ionic diffusion in the carbon micropores, allowing faster charging.

4. Summary and prospect

We have seen that *in-situ* electrochemical characterizations can help elucidate the factors influencing charging mechanisms especially in carbon electrodes for supercapacitors. The capacitance and ion dynamics are significantly affected by charge screening, ionic rearrangements and confinement, and pore features such as ionophilic or ionophobic properties. Presumed ion dynamics includes counterion adsorption, ion exchange, co-ion desorption and potentially many others. Although advances summarized above, more research in the field shall be considered.

Firstly, *in-situ* characterization technique needs improving. The *in-situ* characterizations for supercapacitors are indeed challenging for high power testing, which only takes a few seconds. Long sampling time, *e.g.*, in NMR (~10–10^2 s), has limited the technique from characterizing the quick dynamics. Despite relatively short sampling time, the setup of SAXS or SANS is complex. Well-designed or standardized electrochemical cells are needed for high reproducibility, enhanced signal intensity and introduction of the state-of-the-art spectroscopic techniques. Surface-enhanced Raman spectroscopy (SERS) and shell-isolated nanoparticle-enhanced Raman spectroscopy (SHINERS) have been used to investigate the electrochemical interface, such as for observing the formation of solid electrolyte interphase (SEI) in LIBs [84,85], detecting reversible lithium peroxide (Li_2O_2) and irreversible parasitic products (*i.e.*, LiOH, Li_2CO_3, Li_2O) in Li–O_2 cells [86,87], or revealing the ion adsorption process on metal electrodes [88,89]. SERS and SHINERS can be used in supercapacitors to detect the adsorption species in EDLC and reaction products in pseudocapacitors with higher time and spatial resolutions. On the other hand, free electron laser (FEL) can produce coherent soft and hard X-rays with high brightness, which is nearly ten orders of magnitude higher than that of conventional synchrotron sources, with a pulse duration from 500 to less than 10 fs [90–93]. Abundant information could be achieved during the supercapacitor operation if the emerging FEL could be adopted as laser sources in the *in-situ* spectroscopy for electrode materials. Combining two or more spectroscopic techniques may be also valuable. For instance, *in-situ* X-ray transmission (XRT) and SXAS can reveal distinct factors in the charge storage mechanism [70].

Secondly, theoretical modeling and computational simulation provide an effective way to understand the ion dynamics. A series of capacitors and resistors have been used to construct a range of circuits in the transmission line model, for modelling of both high- and low-frequency responses in charge transport [94], although the matching between model and experimental needs improving [95]. Molecular dynamics (MD) and classical dynamic density functional theory (DFT) may elucidate the charging mechanisms of single or multiple nanopores, but the predicted relaxation time scale and spatial scale are smaller than experimentally measured values. Therefore, combining theoretical modeling with experimental model is a very sensible approach to resolve complex structures. For example, single layer graphene films [75] or graphene stacking with controllable layer spacing [96] could be used as models to investigate the ion fluxes and adsorption in charging and discharging by MD simulation and corresponding electrochemical measure.

Although not focused in this short review, searching for new materials with enhanced electrochemical performance is still crit-

ical, but would bring more puzzles on the mechanisms. MXenes, metal nitrides, metal organic frameworks (MOFs), covalent organic framework (COFs), black phosphorus, and transition-metal dichalcogenides have been examined for their potential in energy storage [1–3]. A recent progress on the graphene membrane supercapacitor indicates the importance of interlayer distance for two-dimensional materials [97]. Pseudocapacitance can be further enhanced by heteroatom doping, *e.g.*, in B/N co-doped [98], or N/S co-doped graphene [99], due to modified electronic structure. Supercapacitors may also be integrated with other devices to build multifunctional self-charging wearable systems. For example, Liu et al. designed a flexible solar-charging integrated unit based on the design of printed magnesium ion aqueous asymmetric supercapacitors [100]. With traditional or newly developed application integrated together with supercapacitors, the understanding of energy storage mechanisms is even more important and challenging, calling further development of *in-situ* techniques.

Declaration of Competing Interest

The authors declare that they have no known competing financial interests or personal relationships that could have appeared to influence the work reported in this paper.

Acknowledgments

This work was supported by the National Natural Science Foundation of China (grant Nos. 51322204 and 51772282).

References

[1] H. Sun, J. Zhu, D. Baumann, L. Peng, Y. Xu, I. Shakir, Y. Huang, X. Duan, Nat. Rev. Mater. 4 (2019) 45–60.
[2] T. Wang, H.C. Chen, F. Yu, X.S. Zhao, H. Wang, Energy Storage Mater. 16 (2019) 545–573.
[3] P. Simon, Y. Gogotsi, Nat. Mater. 7 (2019) 845–854.
[4] L. Dong, C. Xu, Y. Li, Z.H. Huang, F. Kang, Q.H. Yang, X. Zhao, J. Mater. Chem. A 4 (2016) 4659–4685.
[5] L. Hua, Z. Hui, Y. Sun, X. Zhao, H. Xu, Y. Gong, R. Chen, C. Yu, J. Zhou, G. Sun, W. Huang, Nanoscale 10 (2018) 21006–21012.
[6] F. Béguin, V. Presser, A. Balducci, E. Frackowiak, Adv. Mater. 26 (2014) 2219–2251.
[7] S.K. Shinde, S. Ramesh, C. Bathula, G.S. Ghodake, D.Y. Kim, A.D. Jagadale, A.A. Kadam, D.P. Waghmode, T.V.M. Sreekanth, H.S. Kim, P.C. Nagajyothi, H.M. Yadav, Sci. Rep-UK 9 (2019) 13717.
[8] S. Kong, K. Cheng, T. Ouyang, Y. Gao, K. Ye, G. Wang, D. Cao, Electrochim. Acta 246 (2017) 433–442.
[9] A. Krittayavathananon, P. Iamprasertkun, M. Sawangphruk, Carbon 109 (2016) 314–320.
[10] Y. Zhu, S. Murali, M.D. Stoller, K.J. Ganesh, W. Cai, P.J. Ferreira, A. Pirkle, R.M. Wallace, K.A. Cychosz, M. Thommes, D. Su, E.A. Stach, R.S. Ruoff, Science 332 (2011) 1537–1541.
[11] X. Yang, C. Cheng, Y. Wang, L. Qiu, D. Li, Science 341 (2013) 534–537.
[12] Z. Zhou, T. Liu, A.U. Khan, G. Liu, Sci. Adv. 5 (2019) eaau6852.
[13] G. Xiong, P. He, Z. Lyu, T. Chen, B. Huang, L. Chen, T.S. Fisher, Nat. Commun. 9 (2018) 790.
[14] Q. Zhang, K. Han, S. Li, M. Li, J. Li, K. Ren, Nanoscale 10 (2018) 2427–2437.
[15] M. Liu, J. Niu, Z. Zhang, M. Dou, F. Wang, Nano Energy 51 (2018) 366–372.
[16] R. Farzana, K. Hassan, V. Sahajwalla, Sci. Rep-UK 9 (2019) 8982.
[17] Z.S. Wu, D.W. Wang, W.C. Ren, J.P. Zhao, G.M. Zhou, F. Li, H.M. Cheng, Adv. Funct. Mater. 20 (2010) 3595–3602.
[18] Z.S. Wu, W.C. Ren, D.W. Wang, F. Li, B.L. Liu, H.M. Cheng, ACS Nano 4 (2010) 5835–5842.
[19] S. Chen, J.W. Zhu, X.D. Wu, Q.F. Han, X. Wang, ACS Nano 4 (2010) 2822–2830.
[20] J. Yan, Z.J. Fan, T. Wei, W.Z. Qian, M.L. Zhang, F. Wei, Carbon 48 (2010) 3825–3833.
[21] J. Yan, Z.J. Fan, T. Wei, J. Cheng, B. Shao, K. Wang, L.P. Song, M.L. Zhang, J. Power Sources 194 (2009) 1202–1207.
[22] L. Wei, M. Sevilla, A.B. Fuertes, R. Mokaya, G. Yushin, Adv. Funct. Mater. 22 (2012) 827–834.
[23] J. Yan, T. Wei, W. Qiao, Z. Fan, L. Zhang, T. Li, Q. Zhao, Electrochem. Commun. 12 (2010) 1279–1282.
[24] P. Li, Z. Jin, L. Peng, F. Zhao, D. Xiao, Y. Jin, G. Yu, Adv. Mater. 30 (2018) 1800124.
[25] M. Ghidiu, M.R. Lukatskaya, M.Q. Zhao, Y. Gogotsi, M.W. Barsoum, Nature 516 (2014) 78–81.
[26] M.Q. Zhao, C.E. Ren, Z. Ling, M.R. Lukatskaya, C.F. Zhang, K.L.V. Aken, M.W. Barsoum, Y. Gogotsi, Adv. Mater. 27 (2015) 339–345.
[27] J. Yan, C.E. Ren, K. Maleski, C.B. Hatter, B. Anasori, P. Urbankowski, A. Sarycheva, Y. Gogotsi, Adv. Funct. Mater. 27 (2017) 1701264.
[28] A. Shellikeri, I. Hung, Z. Gan, J. Zheng, J. Phys. Chem. C 120 (2016) 6314–6323.
[29] H. Peng, J. Zhou, K. Sun, G. Ma, Z. Zhang, E. Feng, Z. Lei, ACS Sustain. Chem. Eng. 5 (2017) 5951–5963.
[30] S. Nagamuthu, K.S. Ryu, Sci. Rep.-UK 9 (2019) 4864.
[31] Y. Zhai, Z. Zhu, S. Zhou, C. Zhu, S. Dong, Nanoscale 10 (2018) 3089–3111.
[32] Y. Shao, M.F. ElKady, J. Sun, Y. Li, Q. Zhang, M. Zhu, H. Wang, B. Dunn, R.B. Kaner, Chem. Rev. 118 (2018) 9233–9280.
[33] M. Salanne, B. Rotenberg, K. Naoi, K. Kaneko, P.L. Taberna, C.P. Grey, B. Dunn, P. Simon, Nat. Energy 1 (2016) 16070.
[34] W. Guo, C. Yu, S. Li, Z. Wang, J. Yu, H. Huang, J. Qiu, Nano Energy 57 (2019) 459–472.
[35] P.R. Jadhav, M.P. Suryawanshi, D.S. Dalavi, D.S. Patil, E.A. Jo, S.S. Kolekar, A.A. Wali, M.M. Karanjkar, J.H. Kim, P.S. Patil, Electrochim. Acta 176 (2015) 523–532.
[36] E. Talaie, P. Bonnick, X. Sun, Q. Pang, X. Liang, L.F. Nazar, Chem. Mater. 29 (2016) 90–105.
[37] A. Noori, M.F. ElKady, M.S. Rahmanifar, R.B. Kaner, M.F. Mousavi, Chem. Soc. Rev. 48 (2019) 1272–1341.
[38] J.Q. Xie, Y.Q. Ji, J.H. Kang, J.L. Sheng, D.S. Mao, X.Z. Fu, R. Sun, C.P. Wong, Energ, Environ. Sci. 12 (2019) 194–205.
[39] J.L.L. Lopez, P.J. Grandinetti, A.C. Co, J. Mater. Chem. A 6 (2018) 231–243.
[40] M. Kühne, F. Börrnert, S. Fecher, M. Ghorbani-Asl, J. Biskupek, D. Samuelis, A. V. Krasheninnikov, U. Kaiser, J.H. Smet, Nature 568 (2018) 234–239.
[41] M. Kuhne, F. Paolucci, J. Popovic, P.M. Ostrovsky, J. Maier, J.H. Smet, Nature Nanotechnology 12 (2017) 895–900.
[42] M.V. Reddy, G.V. Subba Rao, B.V. Chowdari, Chem. Rev. 113 (2013) 5364–5457.
[43] G. Yoon, H. Kim, I. Park, K. Kang, Adv. Energy Mater. 7 (2017) 1601519.
[44] B.K. Jin, L. Li, J.L. Huang, S.Y. Zhang, Y.P. Tian, J.X. Yang, Anal. Chem. 81 (2009) 4476–4481.
[45] C.M. Pharr, P.R. Griffiths, Anal. Chem. 69 (1997) 4673–4679.
[46] C.M. Pharr, P.R. Griffiths, Anal. Chem. 69 (1997) 4665–4672.
[47] Y. Xia, C. Wang, R. Li, M. Fukuto, B.D. Vogt, Langmuir 34 (2018) 8767–8776.
[48] A. Gibaud, J.S. Xue, J.R. Dahn, Carbon 34 (1996) 499–503.
[49] W.Y. Tsai, P.L. Taberna, P. Simon, J. Am. Chem. Soc. 136 (2014) 8722–8728.
[50] F. Blanc, M. Leskes, C.P. Grey, Accounts Chem. Res. 46 (2013) 1952–1963.
[51] S. Engelke, L.E. Marbella, N.M. Trease, M. De Volder, C.P. Grey, Phys. Chem. Chem. Phys. 21 (2019) 4538–4546.
[52] M. Deschamps, E. Gilbert, P. Azais, E. Raymundo Piñero, M.R. Ammar, P. Simon, D. Massiot, F. Béguin, Nat. Mater. 12 (2013) 351.
[53] S.P. Villar, P. Lanz, H. Schneider, P. Novák, Electrochim. Acta 106 (2013) 506–515.
[54] Y. Yao, W. Chen, Y. Du, Z. Tao, Y. Zhu, Y.X. Chen, J. Phys. Chem. C 119 (2015) 22452–22459.
[55] E.J. Crumlin, Z. Liu, H. Bluhm, W. Yang, J. Guo, Z. Hussain, J. Electron Spectrosc. 200 (2015) 264–273.
[56] M.D. Levi, L. Daikhin, D. Aurbach, V. Presser, Electrochem. Commun. 67 (2016) 16–21.
[57] Q. Zhang, M.D. Levi, Y. Chai, X. Zhang, D. Xiao, Q. Dou, P. Ma, H. Ji, X. Yan, Small Methods (2019) 1900246.
[58] A.C. Forse, J.M. Griffin, C.P. Grey, Solid State Nucl. Mag. 89 (2018) 45–49.
[59] N. Fulik, F. Hippauf, D. Leistenschneider, S. Paasch, S. Kaskel, E. Brunner, L. Borchardt, Energy Storage Mater. 12 (2018) 183–190.
[60] J.M. Griffin, A.C. Forse, C.P. Grey, Solid State Nucl. Mag. 74–75 (2016) 16–35.
[61] J.T. Li, Z.Y. Zhou, I. Broadwell, S.G. Sun, Accounts Chem. Res. 45 (2012) 485–494.
[62] F.W. Richey, B. Dyatkin, Y. Gogotsi, Y.A. Elabd, J. Am. Chem. Soc. 135 (2013) 12818–12826.
[63] F.W. Richey, C. Tran, V. Kalra, Y.A. Elabd, J. Phys. Chem. C 118 (2014) (1855) 21846–21855.
[64] M.A. Gebbie, M. Valtiner, X. Banquy, E.T. Fox, W.A. Henderson, J.N. Israelachvili, P. Natl, A. Sci. 110 (2013) 9674.
[65] S. Ramesh, H.M. Yadav, Y.J. Lee, G.W. Hong, A. Kathalingam, A. Sivasamy, H.S. Kim, H.S. Kim, J.H. Kim, Sci. Rep.-UK 9 (2019) 12622.
[66] C. Prehal, D. Weingarth, E. Perre, R.T. Lechner, H. Amenitsch, O. Paris, V. Presser, Energy Environ. Sci. 8 (2015) 1725–1735.
[67] J.L. Bañuelos, G. Feng, P.F. Fulvio, S. Li, G. Rother, S. Dai, P.T. Cummings, D.J. Wesolowski, Chem. Mater. 26 (2014) 1144–1153.
[68] S. Boukhalfa, D. Gordon, L. He, Y.B. Melnichenko, N. Nitta, A. Magasinski, G. Yushin, ACS Nano 8 (2014) 2495–2503.
[69] C. Prehal, C. Koczwara, H. Amenitsch, V. Presser, O. Paris, Nat. Commun. 9 (2018) 4145.
[70] C. Prehal, C. Koczwara, N. Jäckel, A. Schreiber, M. Burian, H. Amenitsch, M.A. Hartmann, V. Presser, O. Paris, Nat. Energy 2 (2017) 16215.
[71] G. Gambarini, C. Birattari, C. Colombi, L. Pirola, G. Rosi, Radiat. Prot. Dosim. 101 (2002) 419–422.
[72] S. Cierjacks, Y. Hino, M. Drosg, Nucl. Sci. Eng. 106 (1990) 183–191.
[73] M.D. Levi, S. Sigalov, D. Aurbach, L. Daikhin, J. Phys. Chem. C 117 (2013) 14876–14889.
[74] M.D. Levi, S. Sigalov, G. Salitra, R. Elazari, D. Aurbach, J. Phys. Chem. Lett. 2 (2011) 120–124.

[75] J. Ye, Y.C. Wu, K. Xu, K. Ni, N. Shu, P.L. Taberna, Y. Zhu, P. Simon, J. Am. Chem. Soc. 141 (2019) 16559–16563.
[76] M.D. Levi, G. Salitra, N. Levy, D. Aurbach, J. Maier, Nat. Mater. 8 (2009) 872.
[77] C. Merlet, C. Péan, B. Rotenberg, P.A. Madden, B. Daffos, P.L. Taberna, P. Simon, M. Salanne, Nat. Commun. 4 (2013) 2701.
[78] A.C. Forse, J.M. Griffin, C. Merlet, J.C. Gonzalez, A.R.O. Raji, N.M. Trease, C.P. Grey, Nat. Energy 2 (2017) 16216.
[79] A.C. Forse, C. Merlet, J.M. Griffin, C.P. Grey, J. Am. Chem. Soc. 138 (2016) 5731–5744.
[80] J.M. Griffin, A.C. Forse, W.Y. Tsai, P.L. Taberna, P. Simon, C.P. Grey, Nat. Mater. 14 (2015) 812.
[81] A.C. Forse, J.M. Griffin, C. Merlet, P.M. Bayley, H. Wang, P. Simon, C.P. Grey, J. Am. Chem. Soc. 137 (2015) 7231–7242.
[82] J.M. Griffin, A.C. Forse, H. Wang, N.M. Trease, P.L. Taberna, P. Simon, C.P. Grey, Faraday Discuss. 176 (2014) 49–68.
[83] H. Wang, A.C. Forse, J.M. Griffin, N.M. Trease, L. Trognko, P.L. Taberna, P. Simon, C.P. Grey, J. Am. Chem. Soc. 135 (2013) 18968–18980.
[84] L.C. Fernandez, D. Bresser, F. Braga, S. Passerini, L.J. Hardwick, Batteries Supercaps 2 (2019) 168–177.
[85] S.H. Felix, Y.H. Chen, J.Y. Liu, J. Rick, B.J. Hwang, J. Power Sources 256 (2014) 324–328.
[86] J.L. Yang, J. Xu, H. Ren, L. Sun, Q.C. Xu, H. Zhang, J.F. Li, Z.Q. Tian, Nanoscale 9 (2017) 6254–6258.
[87] F.S. Gittleson, K.P.C. Yao, D.G. Kwabi, S.Y. Sayed, W.H. Ryu, Y. ShaoHorn, A.D. Taylor, ChemElectroChem 2 (2015) 1446–1457.
[88] G. Cabello, X.J. Chen, R. Panneerselvam, Z.Q. Tian, J. Raman Spectrosc. 47 (2016) 1207–1212.
[89] P. Wang, H. Li, C. Cui, J. Jiang, Chem. Phys. 516 (2019) 1–5.
[90] T. Ishikawa, H. Aoyagi, T. Asaka, Y. Asano, N. Azumi, T. Bizen, H. Ego, K. Fukami, T. Fukui, Y. Furukawa, S. Goto, H. Hanaki, T. Hara, T. Hasegawa, T. Hatsui, A. Higashiya, T. Hirono, N. Hosoda, M. Ishii, T. Inagaki, Y. Inubushi, T. Itoga, Y. Joti, M. Kago, T. Kameshima, H. Kimura, Y. Kirihara, A. Kiyomichi, T. Kobayashi, C. Kondo, T. Kudo, H. Maesaka, X.M. Maréchal, T. Masuda, S. Matsubara, T. Matsumoto, T. Matsushita, S. Matsui, M. Nagasono, N. Nariyama, H. Ohashi, T. Ohata, T. Ohshima, S. Ono, Y. Otake, C. Saji, T. Sakurai, T. Sato, K. Sawada, T. Seike, K. Shirasawa, T. Sugimoto, S. Suzuki, S. Takahashi, H. Takebe, K. Takeshita, K. Tamasaku, H. Tanaka, R. Tanaka, T. Tanaka, T. Togashi, K. Togawa, A. Tokuhisa, H. Tomizawa, K. Tono, S. Wu, M. Yabashi, M. Yamaga, A. Yamashita, K. Yanagida, C. Zhang, T. Shintake, H. Kitamura, N. Kumagai, Nat. Photonics 6 (2012) 540–544.
[91] H.N. Chapman, A. Barty, M.J. Bogan, S. Boutet, M. Frank, S.P. Hau-Riege, S. Marchesini, B.W. Woods, S. Bajt, W.H. Benner, R.A. London, E. Plönjes, M. Kuhlmann, R. Treusch, S. Düsterer, T. Tschentscher, J.R. Schneider, E. Spiller, T. Möller, C. Bostedt, M. Hoener, D.A. Shapiro, K.O. Hodgson, D. van der Spoel, F. Burmeister, M. Bergh, C. Caleman, G. Huldt, M.M. Seibert, F.R.N.C. Maia, R.W. Lee, A. Szöke, N. Timneanu, J. Hajdu, Nat. Phys. 2 (2006) 839–843.
[92] P.R. Ribič, A. Abrami, L. Badano, M. Bossi, H.H. Braun, N. Bruchon, F. Capotondi, D. Castronovo, M. Cautero, P. Cinquegrana, M. Coreno, M.E. Couprie, I. Cudin, M.B. Danailov, G.D. Ninno, A. Demidovich, S. Di Mitri, B. Diviacco, W.M. Fawley, C. Feng, M. Ferianis, E. Ferrari, L. Foglia, F. Frassetto, G. Gaio, D. Garzella, A. Ghaith, F. Giacuzzo, L. Giannessi, V. Grattoni, S. Grulja, E. Hemsing, F. Iazzourene, G. Kurdi, M. Lonza, N. Mahne, M. Malvestuto, M. Manfredda, C. Masciovecchio, P. Miotti, N.S. Mirian, I. Petrov Nikolov, G.M. Penco, G. Penn, L. Poletto, M. Pop, E. Prat, E. Principi, L. Raimondi, S. Reiche, E. Roussel, R. Sauro, C. Scafuri, P. Sigalotti, S. Spampinati, C. Spezzani, L. Sturari, M. Svandrlik, T. Tanikawa, M. Trovó, M. Veronese, D. Vivoda, D. Xiang, M. Zaccaria, D. Zangrando, M. Zangrando, E.M. Allaria, Nat. Photonics 13 (2019) 555–561.
[93] I. Inoue, T. Osaka, T. Hara, T. Tanaka, T. Inagaki, T. Fukui, S. Goto, Y. Inubushi, H. Kimura, R. Kinjo, H. Ohashi, K. Togawa, K. Tono, M. Yamaga, H. Tanaka, T. Ishikawa, M. Yabashi, Nat. Photonics 13 (2019) 319–322.
[94] C. Pean, B. Rotenberg, P. Simon, M. Salanne, J. Power Sources 326 (2016) 680–685.
[95] M. Korpaas, A.T. Holen, R. Hildrum, Int. J. Elec. Power. 25 (2003) 599–606.
[96] C. Cheng, G. Jiang, G.P. Simon, J.Z. Liu, D. Li, Nat. Nanotechnol. 13 (2018) 685–690.
[97] Z. Li, S. Gadipelli, H. Li, C.A. Howard, D.J.L. Brett, P.R. Shearing, Z. Guo, I.P. Parkin, F. Li, Nat. Energy 5 (2020) 160–168.
[98] X. Wang, G. Sun, P. Routh, D.H. Kim, W. Huang, P. Chen, Chem. Soc. Rev. 43 (2014) 7067–7098.
[99] L. Chen, X. Li, C. Ma, M. Wang, J. Zhou, J. Phys. Chem. C 121 (2017) 18344–18350.
[100] Z. Tian, X. Tong, G. Sheng, Y. Shao, L. Yu, V. Tung, J. Sun, R.B. Kaner, Z. Liu, Nat. Commun. 10 (2019) 4913.